

# Calibration of colour gradient bias in shear measurement using CANDELS

X. Er<sup>1</sup>\*, H. Hoekstra<sup>2</sup>, T. Schrabback<sup>3</sup>, V. F. Cardone<sup>1</sup>, R. Scaramella<sup>1</sup>, R. Maoli<sup>4</sup>, M. Vicinanza<sup>1,4,5</sup>, B. Gillis<sup>6</sup>, L. Miller<sup>7</sup>, J. Rhodes<sup>8,9</sup>

<sup>1</sup> I.N.A.F. - Osservatorio Astronomico di Roma, via Frascati 33, 00040 - Monte Porzio Catone, Roma, Italy

<sup>2</sup> Leiden Observatory, Leiden University, PO Box 9513, NL-230 RA, Leiden, the Netherlands

<sup>3</sup> Argelander Institute fuer Astronomie, Auf dem Huegel 71, D-53121 Bonn, Germany

<sup>4</sup> Dipartimento di Fisica, Universita di Roma "La Sapienza", Piazzale Aldo Moro, 00185 - Roma, Italy

<sup>5</sup> Dipartimento di Fisica, Universita di Roma "Tor Vergata", via della Ricerca Scientifica 1, 00133 - Roma, Italy

<sup>6</sup> Royal Observatory, University of Edinburgh, Blackford Hill, Edinburgh EH9 3HJ, UK

<sup>7</sup> Department of Physics, Oxford University, keble Road, Oxford OX1 3RH, UK

<sup>8</sup> Jet Propulsion Laboratory, California Institute of Technology, 4800 Oak Grove Drive, Pasadena, CA 91109, USA

<sup>9</sup> California Institute of Technology, 1200 East California Blvd, Pasadena, CA 91125, USA

Accepted –; received –; in original from 25 March 2017

## ABSTRACT

*Euclid* will image about two billion galaxies that can be used to infer cosmological parameters using weak gravitational lensing. Exploiting the precision afforded by these data relies critically on our ability to correct for instrumental effects, such as the convolution by the point spread function (PSF). A complication is the fact that the optical data are obtained using a broad bandpass (550–920 nm) while the diffraction-limited PSF depends on wavelength. This leads to biases in the recovered galaxy shapes because the colours of galaxies vary spatially. We show that the colour-gradient bias can be determined with high accuracy in simulated noisy data. We also find that higher order image distortions, such as flexion, enhance the bias, which may be relevant for the study of lensing in high density regions. We estimate the size of this colour-gradient biases using multi-band observations from the *Hubble* Space Telescope and find correlations with the colours and sizes of the galaxies, but do not observe a significant dependence with redshift. **We need some concluding remark about the impact for Euclid.**

**Key words:** cosmology, weak lensing, systematics

## 1 INTRODUCTION

The images of distant galaxies are distorted, or sheared, by the tidal effect of the gravitational potential generated by intervening matter, an effect commonly referred to as weak gravitational lensing (e.g. Bartelmann & Schneider 2001, for a detailed introduction). The measurement of the resulting correlations in the shapes can be used to directly infer the statistical properties of the mass distribution in the Universe, which in turn provide constraints on cosmological parameters. Hence weak gravitational lensing by large-scale structure, or cosmic shear, has been identified as a powerful tool for cosmology. The measurement of the signal as a function of cosmological time is sensitive to the expansion history and the growth rate of large-scale structures, and can be used to constrain models for dark energy and modified gravity.

A useful measurement of the cosmic shear signal requires averaging over large numbers of galaxies to reduce the uncertainty caused by the intrinsic ellipticities of galaxies. The result is, how-

ever, only meaningful if biases in the shape estimates are negligible. Various instrumental effects change the observed ellipticities by more than the typical lensing signal, which is of order one per cent. The most dominant source of bias is the smearing of the images by the point spread function (PSF), driving the desire for space-based observations (??). Despite these observational challenges, the most recent cosmic shear studies are starting to yield competitive constraints on cosmological parameters (????). These results are based on surveys of modest areas of the sky, which limits their ability to study the nature of dark energy, which requires more than an order of magnitude improvement in precision.

Such a measurement is the objective of *Euclid* (Laureijs et al. 2011), the dark energy mission of the European Space Agency (ESA) scheduled for a launch in 2020, which will survey the 15 000 deg<sup>2</sup> of extragalactic sky that has both low extinction and zodiacal light. To reduce the detrimental effects of noise on the shape measurements, the images used for the lensing analysis are observed using a wide bandpass (550–920 nm). The much smaller PSF in space-based observations is a major advantage, but the diffraction-limited PSF leads to new complications.

\* er.xinzhong@oa-roma.inaf.it

The most prominent one is that the correction for the smearing by the chromatic PSF depends on the spectral energy distribution (SED) of the galaxy of interest (Cypriano et al. 2010; ?) and ignoring this would lead to significant biases in the case of *Euclid*. Fortunately this can be accounted for using the supporting broadband observations that are used to derive photometric redshifts for the sources: the correction employs an effective PSF which is derived from the estimate of the observed SED of the galaxy. This correction is sufficient if the SED does not vary spatially (?). If this is not the case, the underlying brightness distribution, which is needed for an unbiased estimate of the shear, cannot be unambiguously recovered from the observed images. This results in a higher order systematic bias, which we call colour-gradient (hereafter CG) bias. As shown by Semboloni et al. (2013) (ES13 in the rest of this paper) the amplitude depends on several factors: the SED of the galaxy, the relative size of the galaxy to the PSF, and the width of the bandpass,  $\Delta\lambda$ . For instance, the bias scales as  $\Delta\lambda^2$ , and thus is particularly relevant in the case of *Euclid*.

Galaxies show a wide variety in colour gradients, with elliptical galaxies typically showing negative colour gradients (redder in the centre and bluer in the outskirts), with steeper gradients more commonly found in bluer or more luminous early type galaxies (e.g. den Brok et al. 2011; Gonzalez-Perez et al. 2011). La Barbera et al. (2010); Kennedy et al. (2016) also suggest correlations between colour gradients and the overall colours and luminosities of the galaxies. Hence the relation between galaxy morphology and density may cause the CG bias to vary across the sky and lead to correlations with the lensing signal itself.

It is important that all systematic sources of biases are accounted for to a level that is smaller than the statistical uncertainties. In the case of *Euclid* this leads to tight requirements, as detailed in (e.g. Cropper et al. 2013; Massey et al. 2013). Initial studies by Voigt et al. (2012) and ES13 used simulated images to show that the CG bias could be substantial, exceeding nominal requirements for the multiplicative bias in the shear. They also argued that it should be possible to calibrate the bias using *Hubble* Space Telescope (HST) observations of a large sample of galaxies in the F606W and F814W filters. However, their conclusion is based on the analysis of simulated noiseless data. In this work, we revisit the issue of the calibration of CG bias, with a particular focus on determining the bias from data with realistic noise levels.

In Section 2, we describe the main concepts and introduce the notation. We present the results from the analysis of simulated images in Section 3. In particular we explore the impact of having to use noisy data to measure the CG bias in Section 3.1. In Section 4 we estimate the CG bias using HST observations from the Cosmic Assembly Near-infrared Deep Extragalactic Legacy Survey (CANDELS; ?).

## 2 THE ORIGIN OF COLOUR GRADIENT BIAS

Following the notation of ES13, we consider an image of a galaxy, and denote the photon brightness distribution of the image at each position  $\theta$  and wavelength  $\lambda$  by  $I(\theta; \lambda)$ , which is related to the intensity  $S(\theta; \lambda)$  by  $I^0(\theta; \lambda) = \lambda S(\theta; \lambda) T(\lambda)$ , where  $T(\lambda)$  is the normalised transmission. We take this to be a top-hat with a width  $\Delta\lambda$  around a central wavelength  $\lambda_{\text{cen}}$ . The resulting image of the galaxy, observed using a telescope with a PSF  $P(\theta; \lambda)$  is given by:

$$I^{\text{obs}}(\theta) = \int_{\Delta\lambda} I^0(\theta; \lambda) * P(\theta; \lambda) d\lambda, \quad (1)$$

where  $*$  denotes a convolution.

A measurement of the ellipticity of a galaxy provides an unbiased (but noisy) estimate of the weak gravitational lensing signal, quantified by the complex shear  $\gamma = \gamma_1 + i\gamma_2$ . The ellipticity  $\epsilon$  in turn can be determined from the second order brightness moments  $Q_{ij}^0$  of the PSF-corrected image  $I^0(\theta)$  (Bartelmann & Schneider 2001):

$$\epsilon_1 + i\epsilon_2 \approx \frac{Q_{11}^0 - Q_{22}^0 + 2iQ_{12}^0}{Q_{11}^0 + Q_{22}^0 + 2(Q_{11}^0 Q_{22}^0 - (Q_{12}^0)^2)^{1/2}} \quad (2)$$

where the second order brightness moments are given by<sup>1</sup>

$$Q_{ij}^0 = \frac{1}{F} \int I^0(\theta) \theta_i \theta_j d^2\theta \quad (i, j = 1, 2), \quad (3)$$

where  $F = \int d^2\theta I^0(\theta)$  is the total observed photon flux.

In practice, however, the observed moments are measured from the PSF-convolved image given by Eqn. (1). Moreover, the moments are evaluated using a weight function  $W(\theta)$  to reduce the effect of noise in the images. Hence, the observed quadrupole moments are given by

$$Q_{ij}^{\text{obs}} = \frac{1}{F_w} \int_{\Delta\lambda} d\lambda \int d^2\theta I^0(\theta; \lambda) * P(\theta, \lambda) \theta_i \theta_j W(\theta), \quad (4)$$

where  $F_w$  is the weighted flux. The use of a weight function biases the observed moments, and the aim of moment-based shape measurement algorithms is to correct for this using estimates of the higher order moment (e.g. Kaiser et al. 1995; Melchior et al. 2011). An alternative approach is to fit sheared, PSF-convolved models to the observed images (e.g. ??); in these fitting methods the profile itself acts as a weight.

ES13 showed that the inevitable use of a weight function gives rise to the CG bias, which scales as  $\Delta\lambda^2$ . The bias also depends on the choice of the weight function, and vanishes in the case of *unweighted* moments. In the latter case it is possible to determine the PSF-corrected moments  $Q_{ij}^0$  from the observed quadrupole moments because

$$Q_{ij}^{\text{obs}} = Q_{ij}^0 + P_{ij}^{\text{eff}} \quad (5)$$

where  $P_{ij}^{\text{eff}}$  are the quadrupole moments of the effective PSF, defined as

$$P_{\text{eff}}(\theta) = \frac{1}{F} \int d\lambda P(\theta, \lambda) F(\lambda), \quad (6)$$

where  $F(\lambda)$  is the photon flux as a function of wavelength, which is directly related to the spectral energy distribution (SED) of the galaxy. Hence the correction for the chromatic PSF requires an estimate of the SED. ? have shown that the broadband observations that are used to determine photometric redshifts for *Euclid* can also be used to estimate the effective PSF with sufficient accuracy to meet the stringent requirements presented in ?.

The observed image is the convolution of the original wavelength-dependent image and a chromatic PSF that is integrated over a wide range in wavelength. This last step prevents the unique recovery of the original image: different original images can appear identical once observed using a broad pass-band. But the response to an applied shear depends on the surface brightness distribution of the original image.

In the following we closely follow the approach of ES13 to

<sup>1</sup> We implicitly assume that the moments are evaluated around the position where the dipole moments vanish.

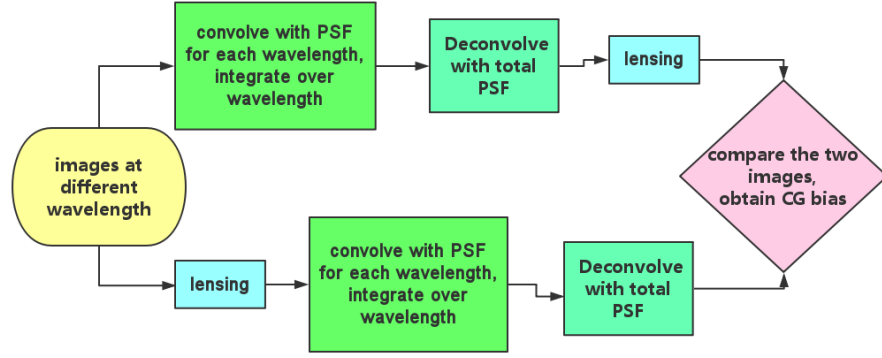


**Figure 1.** Flowchart describing how the colour-gradient bias is determined. The initial image is the same in both flows, but in the top flow an image without a colour gradient is created to which a shear is applied. In the bottom flow, the image is sheared before the PSF steps are applied. The ellipticities of the resulting images differ slightly, and can be used to quantify the bias that is introduced.

evaluate the multiplicative bias in the lensing signal that is introduced by colour gradient.

To quantify the CG bias we compare how the response to an applied shear differs between a galaxy that has no colour gradient and one

Figure 1 shows the flowchart of the steps that enable us to evaluate the CG bias. This nicely shows that the bias is the consequence of the fact that the shearing of the image does not commute with the convolution with the PSF. In both cases we start with the same wavelength dependent image  $I^0(\theta; \lambda)$ , but the bottom flow resembles what happens in the actual observations: the original image is sheared before the convolution with the PSF. The deconvolution with the effective PSF then yields the PSF-corrected shape. In the top flow the PSF steps are applied first, resulting in an image without a colour gradient that is subsequently sheared. The ellipticities of the resulting images provide an estimate of the multiplicative CG bias,  $m$ , via

$$m = \frac{e_i^{CG}}{e_i^{NCG}} - 1, \quad (7)$$

In this paper, we will limit the method to the brightness moments, and use the circular Gaussian weighting function with the size of half light radius.

The CG bias is estimated from following steps: we first generate the image in every wavelength from the galaxy model. Then we shear the images, and apply the convolution with PSF before integrating over the wavelength. Since both the galaxy and the PSF are chromatic, the integrated image contains CG bias. We also need a flat SED image, which contains non-colour gradient (NCG), and is the ideal image for shear measurement. The NCG images can be generated by

$$I^{NCG}(k, \lambda_{ref}) = \frac{F(\lambda_{ref})I^{obs}(k)}{P_{\text{eff}}}, \quad (8)$$

where  $I^{obs}(k)$  is the galaxy image (Eq.1) in Fourier space.

which is the PSF integrated over the filer band. The NCG images are the uniform image over the wavelength. One can see Fig. 1 for the steps of generating the CG and NCG images. In reality, the only difference is that if the lensing process is behind the PSF convolution. We need to emphasize here that the image pair we generated to estimate the CG bias are independent of the measurement method. The bias we will present later are based on the moment

method. As we will shown in the appendix, in the moment method, if we convolve the two images with the same PSF, the ratio of the ellipticity from two images does not change significantly. Comparing the ellipticity (shear) measured from the two images we will have the multiplicative CG bias (Heymans et al. 2006)

$$m = \frac{e_i^{CG}}{e_i^{NCG}} - 1, \quad (9)$$

where  $e_i$  refers to the measurement of the first or second component of the ellipticity. In principle, the two components  $e_1$  or  $e_2$  will give the same estimation of the CG bias. Due to the intrinsic shape of the galaxy images, the two components may have a different response, which can be avoided by rotating the galaxy images. In this work, we will use one ellipticity component  $e_1^{CG}/e_1^{NCG} - 1$  as our estimate if not specified. The additive bias can be detected by correlating the estimated shear and will not be considered here.

### 3 COLOUR GRADIENT BIAS IN SIMULATED DATA

The CG bias is a higher order systematic bias, the numerical noise in simulated images may cause extra error in our analysis. Thus, we first adopt two independent codes to generate the simulated images: one is C/C++ and the other is python-based GalSim package (Rowe et al. 2015). In the C code, we directly calculate the brightness density at the centre of each pixel, and sample the image using the approximate brightness in each pixel (brightness at the centre multiply the area of pixel). In GalSim the image are sampled by FFT rendering. The simulated images are checked for numerical errors, no significant problems are found in neither C or GalSim. Since the deconvolution is particularly difficult in the numerical calculation, we also perform that for the elliptical images. A small relative error  $\sim 10^{-6}$  appears in ellipticity using both C and GalSim, which is two orders of magnitude smaller than the possible CG bias, and can be neglect in this study.

We apply the two same galaxy models as in ES13. It will allow us to further check the numerical error, since in ES13 the images are simulated by different code. The images are consist of two components: bulge and disk, both are modeled by a Sersic profile with index  $n$

$$I_{\text{Sersic}}(\theta) = I_0 e^{-\kappa \theta^{1/n}}, \quad (10)$$

PSF	Description
Gaussian	Gaussian PSF described by Eq. 11 with $w_{0,800} = 0.102$
GaussianT	Gaussian core described by Eq. 11 with $w_{0,800} = 0.054$ plus top-hat with 20 percent of the total flux the cut-off size $\propto \lambda^{0.74}$ (ES13)
Airy	Airy model with obscuration 1/3 (Eq.12)

**Table 1.** The PSF models shown in Fig. 2. The Gaussian model, which is the same PSF model in ES13 is used for the simulated images. The GaussianT model is a Gaussian core plus a top hat function (ES13), which is shown as a comparison with Airy model. The Airy model is used for the bias calibration and HST data analysis in the following section.

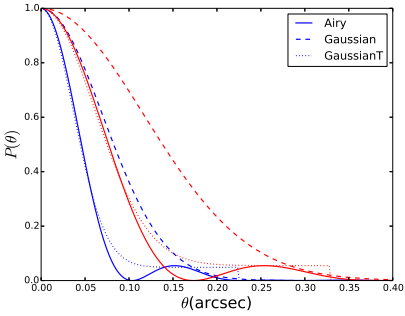


**Figure 2.** Comparison of the PSF models at 550nm (blue) and 920nm (red): the solid, dashed and dotted lines are the Airy, Gaussian and GaussianT PSF models respectively (Table 1).

where  $I_0$  is the central intensity, and  $\kappa = 1.9992 n - 0.3271$ . For the SED of the bulge and the disk we use the galaxy templates from Coleman et al. (1980). The SED of the bulge is modeled by an elliptical galaxy, and SED of irregular galaxy for the disk. We choose an extremely blue SED for disk to generate large colour gradient in the galaxy images. For each wavelength, we construct the galaxy image  $I(\theta, \lambda)$  by adding up the profiles of bulge and disk normalised by fixing the ratio  $S_{bulge}/S_{disk}$  at  $\lambda = 550\text{nm}$ . The integrated profile is applied to the Euclid filter in a wavelength range [550 : 920]nm with a step of 1nm. The images are constructed in an isolated stamp with size  $256 \times 256$  pixels, and resolution 0.05 arcsec/pixel (Table 2).

We use different reference PSF models. The first one is a Gaussian profile, with wavelength dependent width:

$$\sigma_{psf}(\lambda) = w_{0,800} \left( \frac{\lambda}{800\text{nm}} \right), \quad (11)$$

where  $w_{0,800}$  is the width of the PSF at 800nm. In this section we use  $w_{0,800} = 0.102$  arcsec, which is the same as in ES13. The other reference model is an Airy function, which is close to the Design profile (Laureijs et al. 2011)

$$P(\theta) = \frac{I_0}{(1 - \epsilon^2)^2} \left( \frac{2J_1(x)}{x} - \frac{2\epsilon J_1(\epsilon x)}{x} \right)^2, \quad (12)$$

where  $I_0$  is the maximum intensity at the center,  $\epsilon$  is the aperture obscuration ratio, and  $J_1(x)$  is the first kind of Bessel function of order one.  $x$  is defined as  $x = \pi\theta/l$ , where  $l = \lambda/D$  is wavelength over diameter ( $\epsilon = 1/3$ ,  $D = 1.2$  for Euclid). In Fig. 2, we compare the Airy model with other PSF models.

We measure the CG bias as a function of weight size (Fig.3). The solid lines are the results from ES13, and the dashed (dotted)

Name	SED	axis(arcsec)	flux ratio (550nm)	Sersic index $n$
B-galaxy	E/Irr	0.17/1.2	1:3	1.5/1.0
S-galaxy	E/Irr	0.09/0.6	1:3	1.5/1.0

**Table 2.** Parameters of simulated galaxies: when two values are quoted in a column, the first refers to the bulge, the second to the disc.

lines are the results using C (GalSim) code. The blue and green lines are the CG bias of small size galaxy (S-galaxy), while the red and purple lines are that of big size galaxy (B-galaxy). One can see that the CG bias from all three different simulated galaxies are consistent, i.e. the numerical error does not introduce significant bias in this study. Thus, in the following of this section, we will only use the GalSim to generate the mock galaxies. The CG bias decreases with the increasing weight size. As the optimal choice to maximize the signal-to-noise ratio is to match the weight function to the size of the source galaxy, we will use the half light radius for the weight function in the following of this paper. For the two mock galaxies, the CG bias with such a weight function is  $0.8 \times 10^{-3}$ ,  $2 \times 10^{-3}$  for B- and S-galaxy respectively. The smaller size galaxies have a larger CG bias, which suggests that the calibration of the CG bias need to take into account of the size as well as the real colour gradient of the galaxy.

Besides shear, there are higher order image distortions in weak lensing, such as flexion (e.g. Goldberg & Natarajan 2002; Bacon et al. 2006). In previous analysis, we only consider the shear effect in the lensing process, while the higher order image distortions also suffer from CG bias as well. In additional tests, we perform the complete lens ray-tracing instead of solely shearing the images. (We only use our C code in this part, since the current version of GalSim only provides shear effect.) We adopt an Singular Isothermal Sphere halo model as the lens model, and vary the configuration within some reasonable range, such as the Einstein radius, and the separation between the lens and the source image (the corresponding shear value varies between about [0.02, 0.1]). We find that the variation of lensing magnitude can cause different CG bias (yellow shadow in Fig.3), and in most time the flexion effect will increase the CG bias. Such effects do not appear if we solely shear the images. However in general case, the cosmic shear has a value about a few percents. We can see that from the bottom boundary of the yellow shadow, the bias are almost the same as that only considering the shear effect. Only in case of the galaxy cluster lensing, galaxy-galaxy lensing, especially in the strong lensing region, when the flexion becomes significant, one has to take into account of such kind of effect.

### 3.1 Calibration of CG bias using simulated HST images

We outline the method that calibrate the CG bias using two bands images, while the details can be found in ES13. We will use two narrow band images to reconstruct the image at each wavelength. For each of the narrow filter the image can be approximated by:

$$I_i(\theta) = \int_{\Delta\lambda_i} T_i(\lambda) I(\theta, \lambda) d\lambda, \quad (13)$$

where  $T(\lambda)$  is the transmission, and  $i = 1, 2$  stand for the two bands. We assume that for each pixel the image can be interpolated linearly:

$$I(\theta, \lambda) \approx I_{\text{inter}}(\theta, \lambda) = a(\theta)\lambda + b(\theta). \quad (14)$$

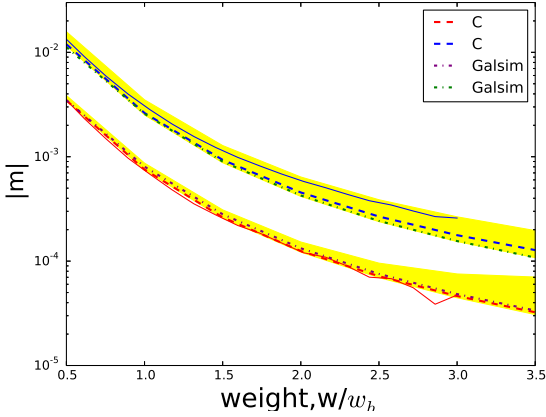


**Figure 3.** The CG bias in shear versus weight function. The solid lines are the results from paper ES13. The dashed (dash-dotted) lines are the results of this work using images simulated from C (GalSim) code. The blue (red) lines are the result for small (big) size simulated galaxies. The yellow shadow is the variation introduced by higher order image distortions.  $w_h$  is half light radius of the galaxy image.

Eqs.13 and 14 yield a linear set of equations on each pixel, which can be used to solved for the coefficients ( $a, b$ ):

$$T_{ai}\lambda a(\theta) + T_{bi}b(\theta) = I_i(\theta), \quad i = 1, 2, \quad (15)$$

where  $T_{ai}, b_i$  is the integrated transmission function at two filters. With ( $a, b$ ) and Eq.14, one can obtain approximated galaxy images of each wavelength  $I(\theta, \lambda)$ . Then we will follow the same procedure as in previous section to estimate the CG bias.

The same two galaxy models from previous section are used in the simulation, and we simulate the images in two HST filters: F606W, F814W, which cover the filter of Euclid image survey. The spectra of the galaxy are shifted according to their redshift, but the evolution of the galaxy or the cosmology are not adopted in the simulation. The spatial resolution is 0.05 arcsec/pixel. The PSF is modeled by the Airy function with diameter  $D = 2.5$  and obscuration 0.33, which is the configuration of HST. As shown in ES13, one needs to correct the PSF effect in the observed images, or the CG bias will be underestimated. We will adopt the same step: deconvolution for images before the bias estimation and discuss that for the noisy images later.

In order to see the effect of noise in the galaxy image, we add Gaussian noise into the simulated HST images. An ideal level (SNR=50) and a moderate level (SNR=15) are used to see the effect of the CG bias. The RMS of the Gaussian image noise is determined by the total flux ( $F_{tot}$ ) within a certain radius  $1.5 r_h$

$$\sigma = \frac{F_{tot}}{\text{SNR}\sqrt{N_{tot}}}, \quad (16)$$

where  $N_{tot}$  is the total pixel number within  $1.5 r_h$ . In Fig.4, we compare the input SNR with that estimated by SExtractor (Bertin & Arnouts 1996). We can see that the estimations are slightly higher than the input values at  $\text{SNR} = 15$ , but still within a reasonable value for real weak lensing survey.

Direct devonvolution of a noisy image will end with a strange galaxy image and large numerical noise, thus we apply Galfit (Peng et al. 2010) to fit the noisy image, and use the fitted image as our noise reduced observed image, i.e. the residual noise is not taken into account for CG analysis. For the necessary fitting profile and number of components, we also use two Sersic components as

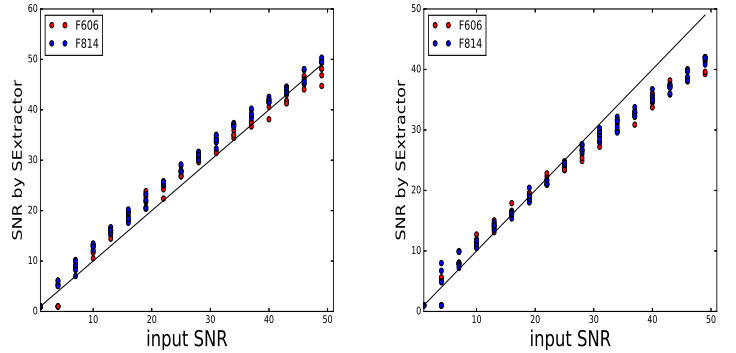


**Figure 4.** SNR estimated by SExtractor vs input SNR. Left is for the B-galaxy; Right is for the S-galaxy.

	S-606W	S-814W	B-606W	B-814W
$n_1$	0.5-2.5	0.5-2.5	0.5-2.5	0.5-2.5
$n_2$	0.5-2.5	0.5-2.5	0.5-2.5	0.5-2.5
$R_{bulge}$	1-10	1-10	3-30	3-30
$R_{disk}$	5-30	5-30	10-60	10-60
$q$	0.6-1	0.6-1	0.6-1	0.6-1

**Table 3.** Constraints for the fitting parameters in Galfit. The first two columns are for two images of the S-galaxy, the other two are the image of B-galaxy.  $n_1$  is the Sersic index for bulge, and  $n_2$  is the Sersic index for disk. The effect radius is given in unit of pixel (0.05 arcsec).

bulge and disk for both image bands. For each image, we apply further constraints to the galaxy parameters: Sersic index, effective radius, and axis ratio (Table 3).

In order to provide a initial parameters for Galfit, we use the stacked image of two bands to estimate the center and some initial values of the galaxy parameters from SExtractor. The fitting images slightly depend on the initial values, and can change the estimate for the CG bias estimation. The dependence will become significant with the decreasing of image SNR. In the following estimation for the CG bias, we will perform the image fitting using two kinds of initial parameters: in the first one we will leave all the fitting parameters free; while in the other one we will freeze the Sersic index as the simulated value, and leave the others free. As we will present, with sufficient large samples, the estimation using noisy images for the CG bias can converge, and is independent of the initial parameters.

Applying the calibration method to the fitted images, we can obtain the estimation of the CG bias for the simulated images. In Figs.5 and 6, we show the shear CG bias with redshift. In each panel, we show different estimates for the bias:

- The black solid lines are the “True” CG bias: we use the true SED of the galaxy and images of each wavelength to estimate the bias without approximation.
- The dashed lines are the estimation using two HST images without noise.
- The colour lines are those using noisy images. The difference between red and blue lines are in the image fitting: for the red lines, we free all the parameters in image fitting, for blue lines we fix the Sersic index as the input value. For the orange lines we also free all the parameters, but we perform another convolution with

the effective PSF (see appendix for more detail). In Fig.1 one can see that the convolution is canceled with the last deconvolution for the CG images. The reason for that is the deconvolution may cause some numerical errors, especially for the small size noisy images. The extra PSF convolution will not significantly change the CG bias as we will show in the appendix. Therefore, in the following result for noise images, we will perform the convolution to the NCG image instead of deconvolution to the CG one.

Moreover, although we use the circular source image in the simulation, the fitted noisy images will become slightly elliptical. In order to get rid of the error due to the “intrinsic shape”, we rotate the source image 6 times, and use the average value as our estimate for the galaxy ellipticity (Nakajima & Bernstein 2007). At each redshift, we use one noise free image and 40(200, 300) noisy images for  $SNR = 50$ ( $SNR = 15$ ). In the bottom panel of each figure, we also show the residues with respect to the true CG bias, and the error bars, which are given by the standard deviation from  $e_{cg}$  and  $e_{ncg}$

$$\sigma_m = |m| \sqrt{\left( \frac{\sigma_{cg}}{\langle e_{cg} \rangle} \right)^2 + \left( \frac{\sigma_{ncg}}{\langle e_{ncg} \rangle} \right)^2}. \quad (17)$$

In the error panel, the grey shadow stands for the error budget of CG bias in Euclid cosmic shear analysis ( $\pm 0.00025$  Cropper et al. 2013; Massey et al. 2013).

One can see that in general our estimate can reproduce the properties of CG bias in ellipticity measurement using both ideal or noisy images. In the high SNR cases (Fig.5), all the estimates with different initial parameters basically agree with each other. The estimate with all fitting parameters free gives lower bias than that fixed the Sersic index. In the low SNR case (Fig.6), the fitting using all free parameters show better estimates for the CG bias, and the residual are within the requirement for most cases. The variance due to the image fitting with different initial parameters are larger than high SNR cases, but can still be reduced by large sample of images and reach the requirement. It means that for each single type of galaxy, one need about 300 galaxy images in order to calibrate the bias. The scatters in the estimation are proportional to the magnitude of the bias, i.e. we have large uncertainty for S-galaxy at low redshift. We also perform tests using images with lower SNR, and calculate the average residue with respect to true bias. When the SNR of images drop to 12, the average residue increases by about 70%(60%) for small(big) galaxy than that of  $SNR = 15$ . This test may not reflect the real dependence on the SNR of images, since in general the lower SNR, the smaller the image size. Therefore, image simulation with specific configuration of the survey is necessary, e.g. the limit magnitude, the population of the galaxies and the relation between the size and SNR etc. In additional tests using other measurement methods for PSF correction, such as the image fitting methods (e.g. Miller et al. 2007; Kitching et al. 2008; Miller et al. 2013), and KSB+ (e.g. Hoekstra et al. 1998; Heymans et al. 2006), we find that the bias has similar dependence on the SED of the galaxies, but with different amplitude.

In both two figures, we notice that at  $z = 0.5$  and  $0.9$ , the estimates are significantly smaller than the true bias for both galaxy models. This is due to the uneven SED of the source galaxy in the two HST filter. In Fig.7, we compare the SED of the galaxy in redshift  $z = 0, 0.5$ . One can see that at  $z = 0.5$ , besides the strong emission lines, the linear approximation cannot reflect the properties of the source galaxies. Thus for some galaxies with complex properties, two band image may not be sufficient to calibrate the CG bias.

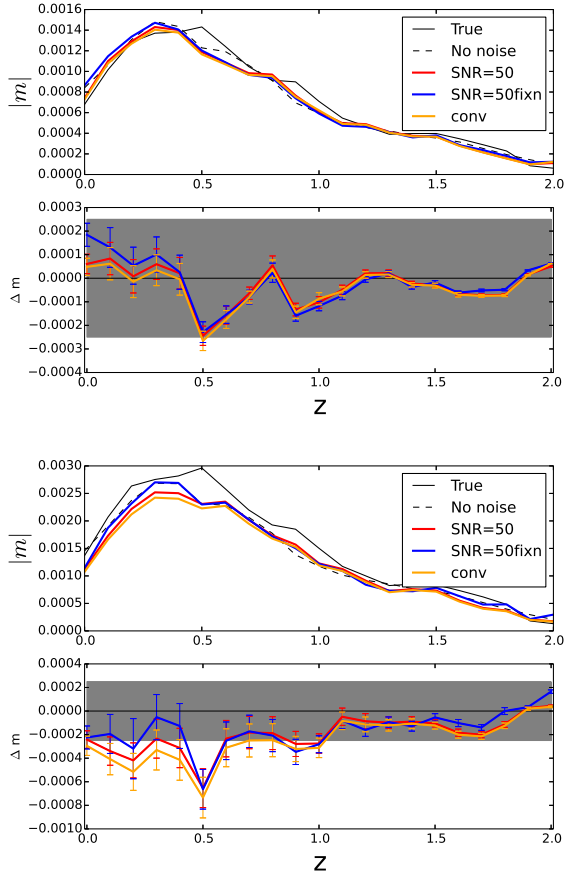


**Figure 5.** The CG bias in shear measurement as a function of redshift using simulated images. The black solid lines are the true CG bias; the dashed lines are the estimation using two band HST images without noise; the colour lines are the estimation using noisy images of input  $SNR = 50$ , the value are the average over 40 realizations each redshift. In the bottom,  $\Delta m$  is the residual with respect to the true CG bias, and the error bars show the standard variations (Eq.17). Up(Down)-figure are the results for B-(S)-galaxy.

### 3.2 PSF variations in calibration data from HST

In the previous test, we used an ideal circular symmetric Airy PSF model. It may however cause inaccuracy in our estimation of the CG bias. Thus, we perform additional tests due to the variations of the PSF. The noise free images are used in order to isolate the effects of the PSF. The different PSF models are applied only in the step of deconvolution for the simulated HST images.

First we generate three pairs of PSF model by slightly increasing the size of PSF. The effect on the CG bias is shown in Fig.8. From solid, dashed to dotted lines, we increased the PSF size of the F606 bands; while from red, green to blue lines, we increase the PSF size of the F814 bands. Although the effect due to the two PSF variations depends on the SED of the source galaxy, one can see that increasing the size of the PSF in different bands will cause either an increase or decrease in the CG bias calibration. Once again, we can see that the small galaxies are more sensitive to the variation of PSF.

To test the impact of imperfect PSF modelling, we make two comparisons: Comparing a control set of “actual” PSFs to a mock set of stars using these PSFs, including some unresolved binaries;

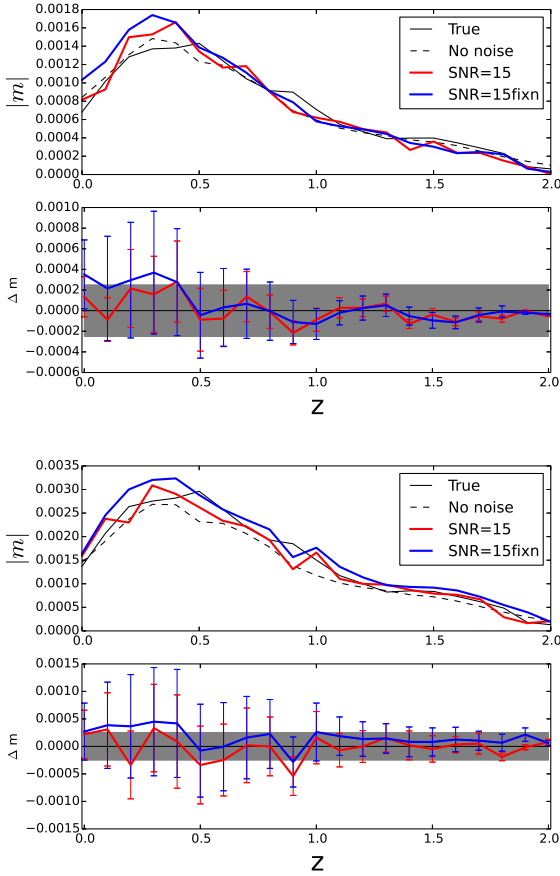


**Figure 6.** Same as Fig.5 but for images of SNR=15. 200 realizations are used for the red lines at each redshift and 220(320) realizations are used for blues lines for the B-(S)-galaxy.

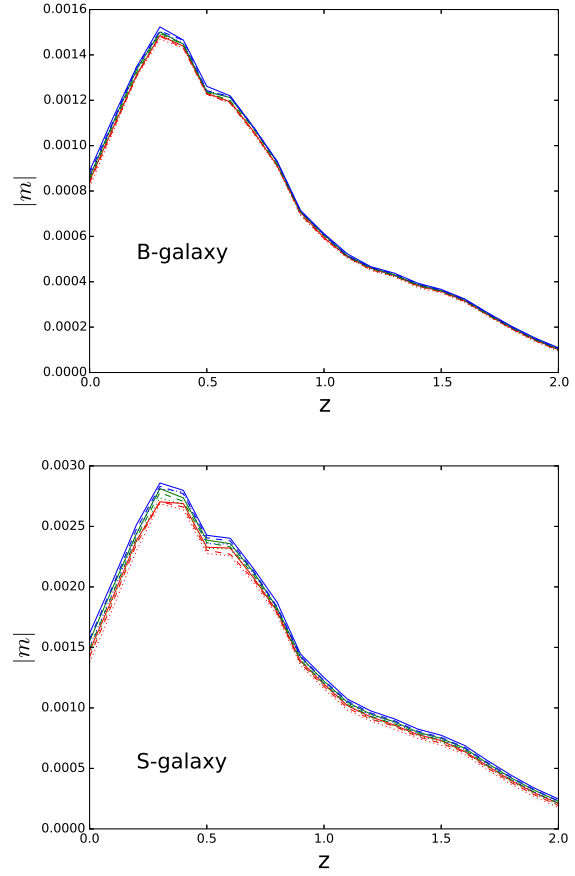


**Figure 8.** The PSF in the deconvolution are varied to see the effect on the CG bias. From red, green to blue lines, we increase the size of PSF for the F814W; from the solid, dashed to dotted lines we increase the size of PSF for the F606W.

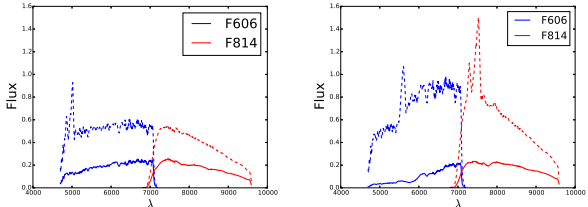


**Figure 7.** Spectral energy distributions used to create the disc and bulge components of our mock galaxies. They are normalized at  $\lambda = 5500\text{\AA}$  by ratio  $F_{\text{bulge}}/F_{\text{disk}} = 1/3$ , and they are convolved with HST filter function in F606W and F814W. *left*- redshift 0; *right*- redshift 0.5.

and comparing the stars in actual images to the best-fit models. In the former case, we generate mock star fields using PSFs generated with the TinyTim tool (Krist et al. 2011) and allow 30 per cent of stars to be unresolved binaries, with another star laid on top of them within a radius of one pixel. In the latter case, we use actual star fields observed with HST and try two methods of fitting the model to the stars. In both cases, we perform this for both the F606W and F814W filters.

The model PSFs are generated using the default parameters for TinyTim where possible, and the appropriate camera, detector, and filter passband settings for each image. For the rest of the options, we use:

- **Position on Detector:** Chosen for each star based on its detected position.

• **Spectrum:** 1; 15 (Use the K7V spectrum, which is chosen to represent a typical star in the sample. The choice of a fixed spectrum for stars was found to have a negligible impact on the models.)

- **PSF Diameter:** 2.0 arcsec

• **Focus-Secondary Mirror Despace:** Fit per image. As HST “breathes” due to its varying angle relative to the Sun, the position of the focus relative to the secondary mirror changes over time and cannot be perfectly predicted for any given observation. We thus have to fit the best focus position by simulating multiple sets of PSFs for each image.

• **Zernike Polynomials:** In the first test, “focus only”, set to default values. In the second test, “all parameters”, these are fit in addition to the focus despace.

- **Subsampling Factor:** 8×

Stars are selected such that they have a signal-to-noise ratio of at least 50, there are no detected objects within 1 arcsecond (20 pixels), and outlier rejection is performed in the fitting procedure. The stars are normalized and then stacked using inverse-variance weighting. The corresponding model PSFs are stacked using the same weights.

In Fig.9, one can see that the inaccuracy of PSF can cause error on the estimation of CG bias. For the small size galaxy, the error

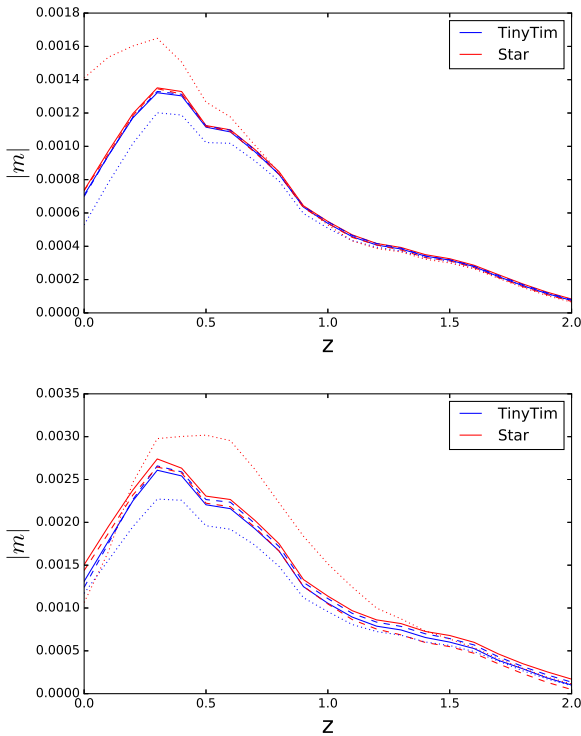


**Figure 9.** Comparison of PSF between TinyTim model and stars. Top (Bottom) is for the B-galaxy (S-galaxy). The solid (dashed) lines are the result using undrizzled (drizzled) PSF. The dotted lines are that if we also include binary PSF effect.

can reach about 15% for undrizzled PSF, while for the big galaxy, the error is only a few percent, can be neglect. In the result using drizzled PSF, the difference becomes smaller. The most problematic PSF will be those from binary stars. One can see for both big and small galaxies, we have a significant error.

## 4 CANDELS DATA

### 4.1 Calibration sample

In this section, we use the real galaxy images to estimate the CG bias which will appear in the Euclid weak lensing survey. For the reference PSF of Euclid, we use the Airy model (Eq. 12), and we use the PSF model from TinyTim for the HST data.

To investigate the impact of colour gradients using realistic galaxies populations, we employ HST/ACS data taken in the F606W and F814W filters in the three CANDELS fields (AEGIS, COSMOS, and UDS), which have a roughly homogeneous coverage in both bands (see Davis et al. 2007; Grogin et al. 2011; Koekemoer et al. 2011). We base our analysis on a tile-wise reduction of the ACS data, incorporating pointings which have at least four exposures to facilitate good cosmic ray removal, yielding combined exposure times of 1.3–2.3ks in F606W and 2.1–3.0ks in F814W. We employ the updated correction for charge-transfer inefficiency from Massey et al. (2014), MultiDrizzle (Koekemoer et al. 2003) for the cosmic ray removal and stacking, as well as careful shift refinement, optimised weighting, and masking for stars and image artifacts as detailed in Schrabback et al. (2010b). Schrabback et al. (in prep.) describe the generation of weak lensing catalogues for these images. We base our analysis on the galaxies passing their

Field	Area (arcmin <sup>2</sup> )	$N_1$	$N_2$	$N_3$
AEGIS	180	2094	2112	3460
COSMOS	139	1593	1656	2449
UDS	146	1455	1497	2341
Total	465	5142	5265	8250

**Table 4.** Size of the HST CANDELS data sample in F606W and F814W bands. The number of galaxies are shown in three selection methods to match the Euclid survey,  $N_1$ :  $m_V < 25$  and  $m_I < 24.5$ ,  $N_2$ :  $m_{VIS} < 24.5$ ,  $N_3$ :  $m_V < 25.5$  and  $m_I < 25$ .

source selection and apply additional magnitude cuts as detailed below. To investigate the dependence of the colour gradient influence on galaxy colour and redshift, we match this galaxy catalogue to the photometric redshift catalogue from Skelton et al. (2014). We list the total non-masked areas in which these catalogues overlap in Table 4.

We match the galaxy from V(F606W) and I(F814W) bands by selecting that the difference of galaxy coordinates in two bands is smaller than 1 pixel (0.05 arcsec). Moreover, in order to resemble the Euclid image survey, we apply selection based on the magnitude of two bands. In the first selection, the galaxy must be brighter than magnitude 25 in V-band and 24.5 in I-band. In the second selection (VIS, N2 sample), we apply the linear interpolation from V and I band using the effective wavelength to approximate the Euclid VIS magnitude, and select the galaxy brighter than 24.5 in VIS. In the last one (N3 sample), we enlarge the sample by using lower threshold in two bands: 25.5 in V and 25.0 in I band. The amount of galaxies is listed in Table4. The galaxy VIS magnitudes will be determined by several factors, such as exposure time and filter transmission, etc. Thus, the actual number of galaxies can be different from what we have shown in this work. The approximation that we use rely on the flatness of the source spectrum. In the VIS sample, the number of galaxies is similar to that in the first selection in all three fields, which suggest that the spectra of our galaxies are relatively smooth. In the N3 sample the galaxy number is much higher. The total galaxy number and number density ( $\sim 12/\text{arcmin}^2$ ) is lower than that in ES13 for several reasons: the galaxies are selected which the 3D-HST photometric redshift are available, and those suitable for weak lensing analysis, e.g. the very big or bright galaxies are not included. Moreover, in ES13 the galaxies are selected by the magnitude of F814W. However we select galaxies by the estimated VIS magnitude and well match in F606W and F814W.

There is no significant difference found in the distribution of galaxy parameters, such as effective radius, axis ratio, photometric redshift and colour (we use  $m_{F606} - m_{F814}$  as colour in this work, and will write as  $m_{V-I}$  later). The SNR of most images in VIS sample are larger than 15, thus they will be able to provide relatively stable estimate for CG bias.

We also compare the galaxies from 3 catalogues (AEGIS, COSMOS, UDS). In the distribution of galaxy parameters (Fig.10), we find no significant difference in half light radius ( $r_h$ ), galaxy axis ratio or redshift distribution. However, in the colour distribution, there are more blue galaxies (small  $m_{V-I}$ ) in AEGIS, which is more significant in N3 sample. We will see later that the colour of galaxy is also related to the CG bias in shape measurement.

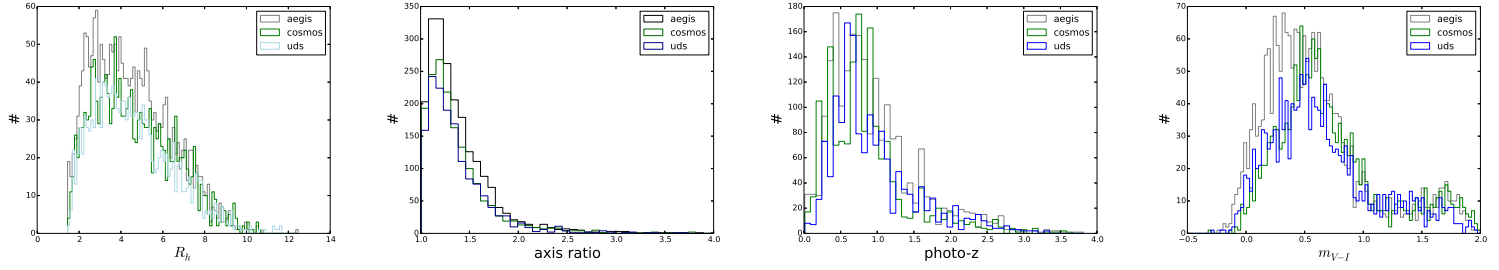


**Figure 10.** The histogram for basic galaxy properties in our sample. The lines with different colours represent galaxies from different catalogues (AEGIS, COSMOS, UDS). From left to right: half light radius, axis ratio, photometric redshift, and colour ( $m_{V-I}$ ).

## 4.2 CG bias from CANDELS

We estimate the CG bias following the same procedure for the simulated galaxy:

- fit the galaxy using one Sersic component for both band images. Some constraints such as Sersic index ( $0.5 < n < 5.0$ ), effective radius ( $1 < r_e < 50$  pixel) and axis ratio ( $0.6 < q < 1.0$ ) are adopted in Galfit.
- interpolate the SED on each pixel of the galaxy image, and generate the galaxy at each wavelength (Eq.13 - 15), and then integrate over the wavelength to simulate the CG and NCG galaxy image.
- measure the shape of two images and calculate the bias  $m$ . We also apply 6 different orientation of the images in order to reduce the intrinsic shape noise.

In Fig.11, we show the histogram of the CG bias. The CG bias in most of the galaxies is smaller than 0.01 (94%). We did not perform averaging as we did for the simulated noisy images, which can further reduce the scatter of the bias. Thus the actual bias, especially the scatter in the sample, is smaller. In the bottom panel, we estimate the CG bias using a larger weight function ( $2r_h$ ). As one expected, the bias decreases by about one order of magnitude.

The colour gradients as a tracer of galaxy evolution have been found to be correlate with some aspects. We try to explore relations between CG bias and the properties of galaxy. First we show the relation between CG bias with two tracers of the colour gradients: the ratio of Sersic index from two bands, and the ratio of effective radius from two bands (Fig. 12). One can see that there is a linear relation between the bias and the radius, but for that of Sersic index it is not obvious. The reason is that the Sersic index is mainly account for the type of the galaxy, the radius correlates with the colour gradient directly. Moreover, the CG bias depends on several factors of the galaxy, e.g. the total size of the galaxy. It is not surprise to see large bias scatters for the whole sample. In principle, one expect that when  $r_{e606} = r_{e814}$  and  $n_{606} = n_{814}$ , the CG bias in principle will be vanish, since the identical images from two bands will not have a colour gradient. This is confirmed in our result: the blue line (bin average) in Fig. 12 meets zero at  $r_{e814}/r_{e606} = 1$ . However, those colour gradients information will not be available in Euclid. We also need the relation between the bias with other parameters.

In Fig.11, the galaxies in AEGIS field have more positive CG bias than the galaxies in the other two. The colour distribution in AEGIS is different from the other two as well, which suggests the correlation between the CG bias and the colour of the galaxy. In Fig.13, we show the relation between the CG bias and the colour of the galaxies. The bias is inversely proportional to the colour of

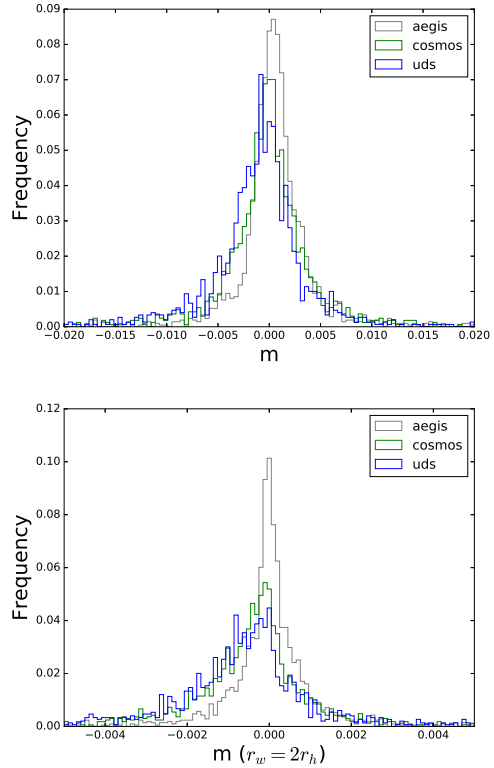


**Figure 11.** CG bias histogram from CANDELS: different colours show the result from three catalogues. In the bottom panel we show the CG bias using different weight function ( $r_w = 2r_h$ ).

the galaxies. This is consistent with the trend of total colour (e.g. Tortora et al. 2010): the bluer galaxies have positive colour gradients, while the redder ones have negative gradients. Since this marks a possible transition of two types of galaxies, we split the galaxy sample into two groups according to their colour: the red galaxies ( $m_{V-I} > 0.5$ ) and the blue ones ( $m_{V-I} < 0.5$ ). They are shown in the bottom panel of Fig.13 as a function of redshift. Most of the red galaxies are located at moderate redshifts, mainly between redshift [0.5, 1.0], while the blue galaxies are either at the lower redshift ( $z < 0.5$ ) or higher redshift ( $z > 1.0$ ). The CG bias in red galaxies are obviously more negative than that of the blue ones. It again confirms that the colour/colour gradients is an important tracer of the galaxy evolution, since apparently galaxies at different redshift proceed at different stages of the evolution.

In addition, we stack the images from two bands as our mock

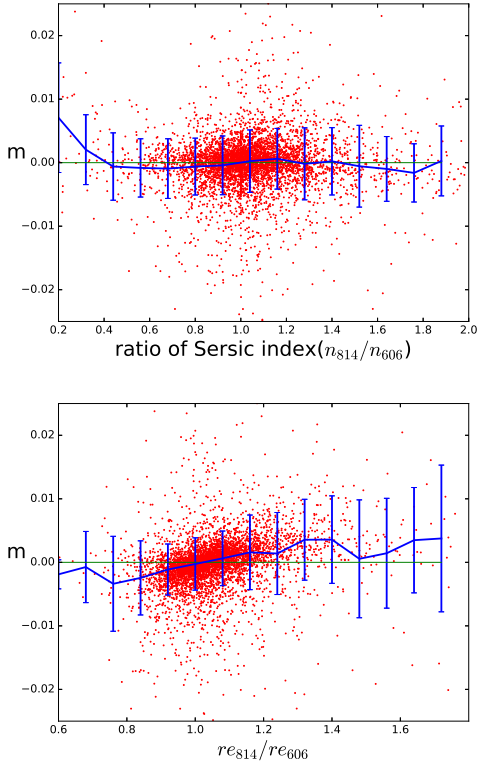


**Figure 12.** CG bias as a function of galaxy properties: ratio of Sersic index between two band (top) and effective radius between two bands (bottom). The blue lines are the average CG bias over the parameter bins.

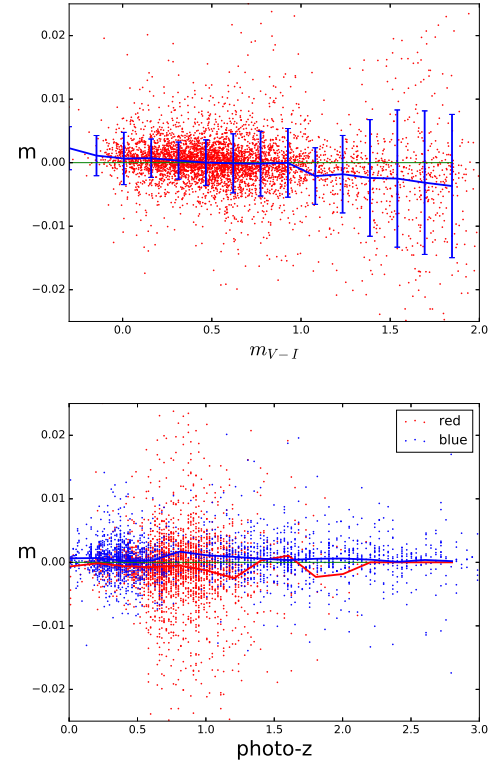


**Figure 13.** CG bias as a function of galaxy properties, top: color ( $m_{V-I}$ ), bottom: photo-z. In the bottom panel, the red and blue points are the bias for red ( $m_{V-I} > 0.5$ ) and blue ( $m_{V-I} < 0.5$ ) galaxies respectively. The lines are the average CG bias in the redshift bins.

VIS band images, together with the mock VIS magnitude ( $m_{VIS}$ ). In Fig.14, we show the bias as a function of  $m_{VIS}$ . There is no obvious dependence on  $m_{VIS}$ , which seems conflict with some study of colour gradients, e.g. Tortora et al. (2010) find tight relation between colour gradients and  $r$ -band magnitude. However, there are two points one needs to notice: 1) the actual  $m_{VIS}$  is different from our linear approximation, also the filter transmission are different of two telescope. 2) the more important thing is that the wide band magnitude may not contain sufficient information about the type or colour of galaxy, thus may not be a good tracer for CG bias.

The VIS image, on the other hand, contains more information. Fig.15 shows the CG bias with the Sersic index and the effective radius fitted from the VIS images. In the top panel, we divide the sample into two groups by the fitted effective radius, either larger or smaller than 0.35 arcsec. The small (large) galaxies are shown by the blue (orange) points, and the blue (red) line is the bin average. The large galaxies cover a large range of Sersic index, have negative average CG bias. Most of small galaxies have small Sersic index ( $< 2.5$ ). The bias of small galaxies are positive and approximately proportional to the Sersic index. The scatters of the bias for both large and small galaxies increase with the Sersic index. In the bottom panel, the galaxies are divide into three groups: the first is red galaxy whose color is large ( $m_{V-I} > 1.0$ ); the second and third group are the rest galaxies either with large Sersic index ( $n > 2.25$ , elliptical galaxy) or small Sersic index (disk galaxy). The solid lines show the bin average over effective radius. We can see that the VIS image alone can also provide an rough estimation for CG bias, but classification of the galaxies is necessary. As shown in the figure, the disk galaxies have small bias, small radius

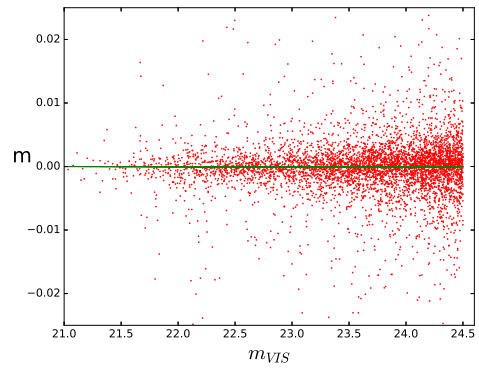


**Figure 14.** CG bias as a function of mock VIS magnitude.

( $< 1$  arcsec), and also small bias scatters. The elliptical galaxies cover large radius range, and the bias is larger than the disk ones. The bias in red galaxies are significant, and mainly negative. The scatters of red galaxies are larger than the other two kinds of galaxies. Extra photometry can definitely provide more constraints on the CG bias, as it has been shown the correlations between colour gradients and other properties of galaxy. Moreover, the multi-band information is required for the photometric redshift study. One can obtain that for free to calibrate the CG bias. Although the dependence on the multi-band is different between photometric redshift and CG bias, the experience from photometric redshift can be used for CG bias, such as some machine learning algorithms.

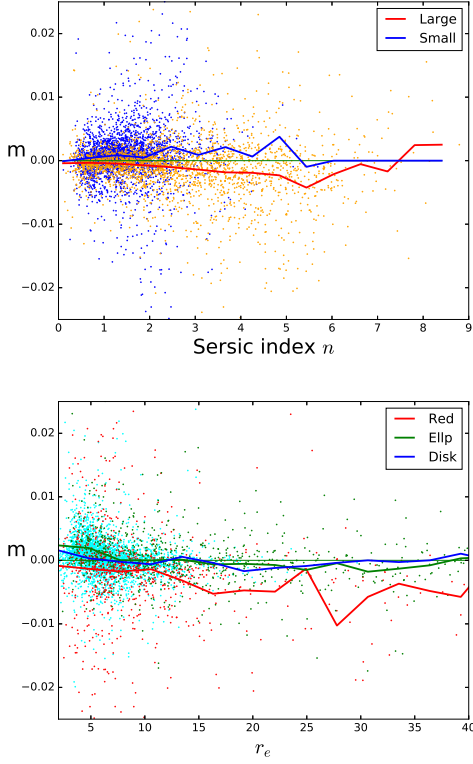


**Figure 15.** CG bias with Sersic index (top) and effective radius (bottom) from the mock VIS images. The unit of radius is a pixel ( $= 0.05 \text{ arcsec}$ ). In the top panel, the blue (red) is the average of small (big) galaxies. In the bottom panel, the red line is average bias of red galaxy ( $m_{V-I} > 1$ ); the green line is that of elliptical galaxy ( $n_{\text{Sersic}} > 2.75$ ); the blue line is for the disk galaxy.

We calculate the average bias and the dispersions over the redshift bins for both red ( $m_{V-I} > 0.5$ ) and blue galaxies (Table 5). The red galaxies are mainly located between redshift (0.4, 1.2), while the blue galaxies are low density in redshift (0.8, 1.2). The bias from red galaxies are significantly smaller than that of blue galaxies, as one expected, the colour gradient in the elliptical galaxies are smaller. The dispersions of the bias in each bin are large, which probably indicate that in each bin there are several kinds and sizes of galaxies. Therefore, in order to calibrate the bias with high precision, one need bigger galaxy samples. From our simulation, we need about 200 galaxies for one type of galaxy in every redshift bin. If we make rough bins, for instance, 2 types of colour: red and blue; 5 different sizes from about 0.1 arcsec to 1.0 arcsec (Fig.15), and 5 redshift bins, at least 20000 galaxies are required. For more realistic SED classifications and redshift bins, several times larger sample are also necessary.

## 5 SUMMARY AND DISCUSSION

In the image survey for weak gravitational lensing, the wide band filter can provide high signal-to-noise images and large coverage of redshift range. There is however a shape bias due to the chromatic shape of galaxy and the PSF, which is named as colour gradient bias. For very wide band surveys, such as Euclid, this effect can

photo-z	Number	$\bar{m}$	$\sigma_m$
0 – 0.4	187	$-1.3 \times 10^{-3}$	0.012
0.4 – 0.8	1415	$-7.6 \times 10^{-4}$	0.011
0.8 – 1.2	1116	$-1.0 \times 10^{-3}$	0.017
> 1.2	245	$-2.1 \times 10^{-3}$	0.015
0 – 0.4	667	$6.6 \times 10^{-4}$	0.0026
0.4 – 0.8	513	$2.8 \times 10^{-4}$	0.0028
0.8 – 1.2	187	$1.2 \times 10^{-3}$	0.0041
> 1.2	935	$5.4 \times 10^{-4}$	0.0046

**Table 5.** The number, average CG bias and dispersion in redshift bins for blue (bottom half) and red (top half) galaxies.

cause a non-negligible bias. In this work, we exam such a kind of bias in measuring the shape of a galaxy using both simulated images and real data taken from the HST ACS CANDELS survey. In the simulated galaxy images, we confirm the bias behaviour from previous results (ES13). We further apply the calibration method to the noisy images in the simulations, and find that with reasonable signal-to-noise ratio (SNR= 15) and sufficient numbers of galaxies (300 images for one type of galaxy in one redshift bin), we can estimate the CG bias to a high precision. However, the underestimate cannot be avoided due to strong emission lines, or the uneven SED of source galaxies. Moreover, the simulations are performed with only two galaxy models, and the SNR of the simulated images in two bands are assigned with equal value. In reality, the relation between the SNR with the size and SED of the galaxies has to be taken into account. We also perform comparison of TinyTim and star PSF models. The inaccuracy, especially that due to the binary stars, will cause errors in estimating the CG bias.

In the estimation using CANDELS data, we select the images from two filters (F606W, F814W). For most of the galaxy, the bias ( $|m|$ ) is smaller than 0.01. As we find from simulated images, the estimation using noisy image has a large scatter, thus the CG bias in reality may be even smaller than that shown here. In our sample of galaxies, the CG bias shows a correlation with the colour of galaxies, and a linear relation with the ratio of two band images. We also generate the mock VIS band images. From the parameters of the image (Sersic index and effective radius), one can classify the galaxy in order to obtain tighter constraints on the bias. For example, the galaxies with small Sersic index, i.e. disk-like, have smaller CG bias. On the other hand, those with large Sersic index have large bias and also bias variation. The relations show consistent results about the colour gradient dependence on the properties of galaxy (e.g. Tortora et al. 2010). However, since the CG bias also depends on the relative size with respect to the PSF, the dependence of CG bias is certainly more complicate. We did not provide any fitting formula for the bias at current sample, since the scatters are too large. More importantly, it has to be performed according to the types or morphology of the galaxies, which require larger sample of data.

The multi-band photometry from several bands, which can be used to estimate the redshift, can be also use for the CG bias analysis. Although the redshift dependence is not significant in our sample of galaxies, this may not be the case for a larger survey, or if we look at the bias according to the type of galaxy. Moreover, the colour of galaxy also indicates the evolution history, or the large scale tide force. It can be also used for the study of intrinsic alignment analysis in weak lensing (e.g. Joachimi et al. 2015). Therefore, the dependence of the CG bias on the colour of the galaxies will further increase the sysmatics of the intrinsic alignment. The detail behaviour will require large cosmological simulations, which

is beyond the scope of this paper, but definitely needs further studies for the project such as Euclid.

The role of environment on the colour gradients is not clear. On the one hand, it has been shown that colour gradients depend on the environment where galaxies reside, with steeper colour gradients in poor rather than rich clusters (e.g. La Barbera et al. 2005), which is possible due to the different processes during galaxy formation. On the other hand, in recent study using integral field spectra from SDSS-IV, the metallicity gradients show weak or no correlation with density environment (Zheng et al. 2017). In any cases, close galaxy pairs or nearby bright star(s) may also cause weak brightness/colour gradient, which will affect our estimate for CG bias as well. Moreover, in the calibration we linearly interpolate the SED on pixels from two bands. Some advanced method to estimate the SED (e.g. Joseph et al. 2016) may help to improve the calibration of the bias.

In this work, we use the brightness moments to estimate the ellipticity of the galaxy. The PSF correction is not taken into account. The bias thus will appear in every method of measurement. However, the bias using the measurement method for real data will be different, since every method has its own property and weight function. The CG bias will have method-dependent properties as well, although they will in principle have same dependence on the colour gradient of the galaxy images. As the first step of the CG bias analysis, we did not adopt any specific method in order to obtain general properties of the CG bias. Before the real analysis of Euclid data, one needs to study the bias with specific methods and simulated images with real properties in the Euclid weak lensing survey.

## ACKNOWLEDGMENTS

We would like to thank Emiliano Merlin, Marco Castellano for helping on SExtractor and Galfit, Gary Bernstein, Adam Rogers and also in general, the members of the Euclid Consortium for useful discussions. XE and VFC are funded by Italian Space Agency (ASI) through contract Euclid -IC (I/031/10/0) and acknowledge financial contribution from the agreement ASI/INAF/I/023/12/0. XE is also partly support by NSFC Grant No. 11473032. JR is supported by JPL, which is run by Caltech under a contract for NASA, and is supported by grant NASA ROSES 12-EUCLID12-0004. The fast Fourier transforms are supplied by the FFTW library (Frigo & Johnson 2005). We use CFITSIO (Pence 1999) for the FITS file.

## REFERENCES

- Bacon, D. J., Goldberg, D. M., Rowe, B. T. P., & Taylor, A. N. 2006, MNRAS, 365, 414
- Bacon, D. J., Refregier, A. R., & Ellis, R. S. 2000, MNRAS, 318, 625
- Bartelmann, M. & Schneider, P. 2001, Phys. Rep., 340, 291
- Bertin, E. & Arnouts, S. 1996, A&AS, 117, 393
- Clowe, D., Bradač, M., Gonzalez, A. H., et al. 2006, ApJ, 648, L109
- Coleman, G. D., Wu, C.-C., & Weedman, D. W. 1980, ApJS, 43, 393
- Cropper, M., Hoekstra, H., Kitching, T., et al. 2013, MNRAS, 431, 3103
- Cypriano, E. S., Amara, A., Voigt, L. M., et al. 2010, MNRAS, 405, 494
- Davis, M., Guhathakurta, P., Konidaris, N. P., et al. 2007, ApJ, 660, L1
- den Brok, M., Peletier, R. F., Valentijn, E. A., et al. 2011, MNRAS, 414, 3052
- Frigo, M. & Johnson, S. G. 2005, Proceedings of the IEEE, 93, 216, special issue on “Program Generation, Optimization, and Platform Adaptation”
- Fu, L., Semboloni, E., Hoekstra, H., et al. 2008, A&A, 479, 9
- Goldberg, D. M. & Natarajan, P. 2002, ApJ, 564, 65
- Gonzalez-Perez, V., Castander, F. J., & Kauffmann, G. 2011, MNRAS, 411, 1151
- Grogan, N. A., Kocevski, D. D., Faber, S. M., et al. 2011, ApJS, 197, 35
- Heymans, C., Van Waerbeke, L., Bacon, D., et al. 2006, MNRAS, 368, 1323
- Hoekstra, H., Franx, M., Kuijken, K., & Squires, G. 1998, ApJ, 504, 636
- Hoekstra, H. & Jain, B. 2008, Annual Review of Nuclear and Particle Science, 58, 99
- Joachimi, B., Cacciato, M., Kitching, T. D., et al. 2015, Space Sci. Rev., 193, 1
- Joseph, R., Courbin, F., & Starck, J.-L. 2016, A&A, 589, A2
- Kaiser, N., Squires, G., & Broadhurst, T. 1995, ApJ, 449, 460
- Kennedy, R., Bamford, S. P., Häußler, B., et al. 2016, A&A, 593, A84
- Kilbinger, M., Fu, L., Heymans, C., et al. 2012, ArXiv 1212.3338
- Kitching, T. D., Balan, S. T., Bridle, S., et al. 2012, MNRAS, 423, 3163
- Kitching, T. D., Miller, L., Heymans, C. E., van Waerbeke, L., & Heavens, A. F. 2008, MNRAS, 390, 149
- Koekemoer, A. M., Faber, S. M., Ferguson, H. C., et al. 2011, ApJS, 197, 36
- Koekemoer, A. M., Fruchter, A. S., Hook, R. N., & Hack, W. 2003, in HST Calibration Workshop : Hubble after the Installation of the ACS and the NICMOS Cooling System, ed. S. Arribas, A. Koekemoer, & B. Whitmore, 337
- Krist, J. E., Hook, R. N., & Stoehr, F. 2011, in Society of Photo-Optical Instrumentation Engineers (SPIE) Conference Series, Vol. 8127, Society of Photo-Optical Instrumentation Engineers (SPIE) Conference Series, 0
- La Barbera, F., De Carvalho, R. R., De La Rosa, I. G., et al. 2010, AJ, 140, 1528
- La Barbera, F., de Carvalho, R. R., Gal, R. R., et al. 2005, ApJ, 626, L19
- Laureijs, R., Amiaux, J., Arduini, S., et al. 2011, ArXiv: 1110.3193
- Massey, R., Hoekstra, H., Kitching, T., et al. 2013, MNRAS, 429, 661
- Massey, R., Schrabback, T., Cordes, O., et al. 2014, MNRAS, 439, 887
- Melchior, P., Viola, M., Schäfer, B. M., & Bartelmann, M. 2011, MNRAS, 412, 1552
- Merten, J., Meneghetti, M., Postman, M., et al. 2015, ApJ, 806, 4
- Meyers, J. E. & Burchat, P. R. 2015, ApJ, 807, 182
- Miller, L., Heymans, C., Kitching, T. D., et al. 2013, MNRAS, 429, 2858
- Miller, L., Kitching, T. D., Heymans, C., Heavens, A. F., & van Waerbeke, L. 2007, MNRAS, 382, 315
- Nakajima, R. & Bernstein, G. 2007, AJ, 133, 1763
- Pence, W. 1999, in Astronomical Society of the Pacific Con-

- ference Series, Vol. 172, Astronomical Data Analysis Software and Systems VIII, ed. D. M. Mehringer, R. L. Plante, & D. A. Roberts, 487
- Peng, C. Y., Ho, L. C., Impey, C. D., & Rix, H.-W. 2010, AJ, 139, 2097
- Rowe, B. T. P., Jarvis, M., Mandelbaum, R., et al. 2015, Astronomy and Computing, 10, 121
- Schrabback, T., Hartlap, J., Joachimi, B., et al. 2010a, A&A, 516, A63
- Schrabback, T., Hartlap, J., Joachimi, B., et al. 2010b, A&A, 516, A63
- Semboloni, E., Hoekstra, H., Huang, Z., et al. 2013, MNRAS, 432, 2385
- Skelton, R. E., Whitaker, K. E., Momcheva, I. G., et al. 2014, ApJS, 214, 24
- Tortora, C., Napolitano, N. R., Cardone, V. F., et al. 2010, MNRAS, 407, 144
- Umetsu, K., Medezinski, E., Nonino, M., et al. 2012, ApJ, 755, 56
- Voigt, L. M., Bridle, S. L., Amara, A., et al. 2012, MNRAS, 421, 1385
- Wittman, D. M., Tyson, J. A., Kirkman, D., Dell'Antonio, I., & Bernstein, G. 2000, Nature, 405, 143
- Zheng, Z., Wang, H., Ge, J., et al. 2017, MNRAS, 465, 4572